ACS APPLIED MATERIALS & INTERFACES

Research Article

www.acsami.org

Mildly Alkaline Preparation and Methylene Blue Adsorption Capacity of Hierarchical Flower-like Sodium Titanate

Miao Feng, Wen You, Zhongsheng Wu, Qidi Chen, and Hongbing Zhan*

College of Materials Science and Engineering, Fuzhou University, 2 Xueyuan Road, Fuzhou 350108, People's Republic of China

Supporting Information

ABSTRACT: The hydrothermal preparation of flower-like layered sodium titanate architectures in a weakly alkaline medium is reported. NaCl was used as a morphology-directing agent, and a growth mechanism was proposed. The hierarchical structure is assembled from one-dimensional nanoribbons and exhibits an excellent removal capacity toward methylene blue (MB). A pseudo-second-order kinetic model was found to well describe the adsorption kinetics. Kinetic studies demonstrated that the overall rate of MB adsorption was controlled by surface adsorption and intraparticle diffusion. Results of this work are of great significance for environmental applications of flower-like layered sodium titanate architectures as a promising adsorbent material used for water purification.

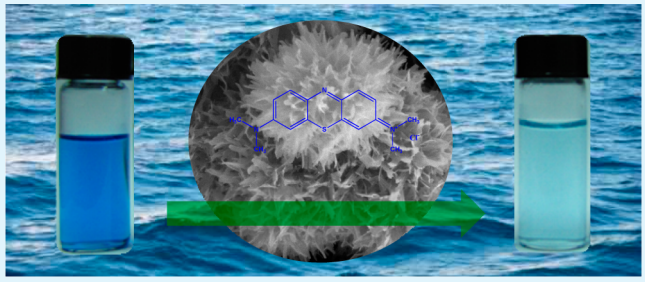

KEYWORDS: *titanate, hydrothermal, sodium chloride, methylene blue, adsorption*

INTRODUCTION

Alkali metal and hydrogen titanates have attracted much recent attention because of their potential in photocatalysis, wastewater treatment, ion exchange, lithium ion storage, gas sensors, and solar energy conversion.[1−6] Numerous methods have been developed for preparing one-dimensional (1D) titanate nanostructures and characterizing their size- and morphology-dependent properties.[7,8] Moreover, alkali metal titanates can be delaminated to form exfoliated two-dimensional (2D) nanosheet/-funnel/-disks, which are useful building blocks for functional materials, such as mesoporous hybrids with high specific surface area and tailored porosity.[9−11] The performance of titanate nanomaterials can be promoted by engineering the morphology of their micro/nanoarchitectures, especially for three-dimensional (3D) hierarchical architectures with low-dimensional building blocks.[12−14] The advantages of nanoscale building blocks and microsized assemblies benefit the resulting structures, which frequently exhibit properties different from those of lower-dimensional structures.

Three-dimensional hierarchical titanate microsized architectures (3D-HTMA) exhibit enhanced absorption compared with their lower-dimensional building blocks and have potential in wastewater treatment.[15,16] On the one hand, 3D-HTMA own the favorable properties of 1D and 2D titanate nanostructures, such as flexible interlayer distances, high cation exchange capacity, and high surface hydroxyl group densities. On the other hand, 3D-HTMA assembled from low-dimensional nanostructures can avoid aggregation, maintain a high dye/metal adsorption contact area, and provide mechanical robustness against flow. These properties result from the hierarchical structure and usually result in higher absorption efficiency.[15]

Many 3D hierarchical titanate structures have been prepared under hydrothermal/solvothermal conditions. Building block morphologies are often nanosheets,[17] wires,[18] tubes,[13] rods,[19] and plates,[20] which can be controlled by the precursor type, reactant ratio, reaction duration, temperature, and the use of surfactants.[21−23] However, these advanced architectures typically require alkaline solution concentrations of ≥5 M to prepare well-organized 3D-HTMA. Tang et al.[22] reported a fast template-free method to prepare high surface area 3D hierarchical layered titanate microspherulite. The product exhibited excellent adsorption capability toward methylene blue (MB) and Pb^{II}, but the NaOH concentration used was 10 M. Excess alkali media entering wastewater systems results in environmental pollution and wasted raw materials. There is little available literature about the hydrothermal synthesis of 3D-HTMA under less aggressive conditions. Hierarchically hollow titanate architectures assembled from titanate nanotubes and nanosheets were recently reported by hydrothermal synthesis under low alkalinity conditions.[17,23] The experimental design itself is simple and intuitive, but its application may be limited by the complicated two-step procedure. An easy, efficient, and environmentally friendly preparation for high-quality 3D-HTMA is required.

With the rapid development of dyestuff industry, the wastewater with high color degree from print and dye plants is considered as the most pernicious industrial wastewater. The removal of color synthetic organic dyestuff from waste effluents becomes environmentally important. MB is a thiazine dye,

Received: September 15, 2013
Accepted: November 18, 2013
Published: November 18, 2013

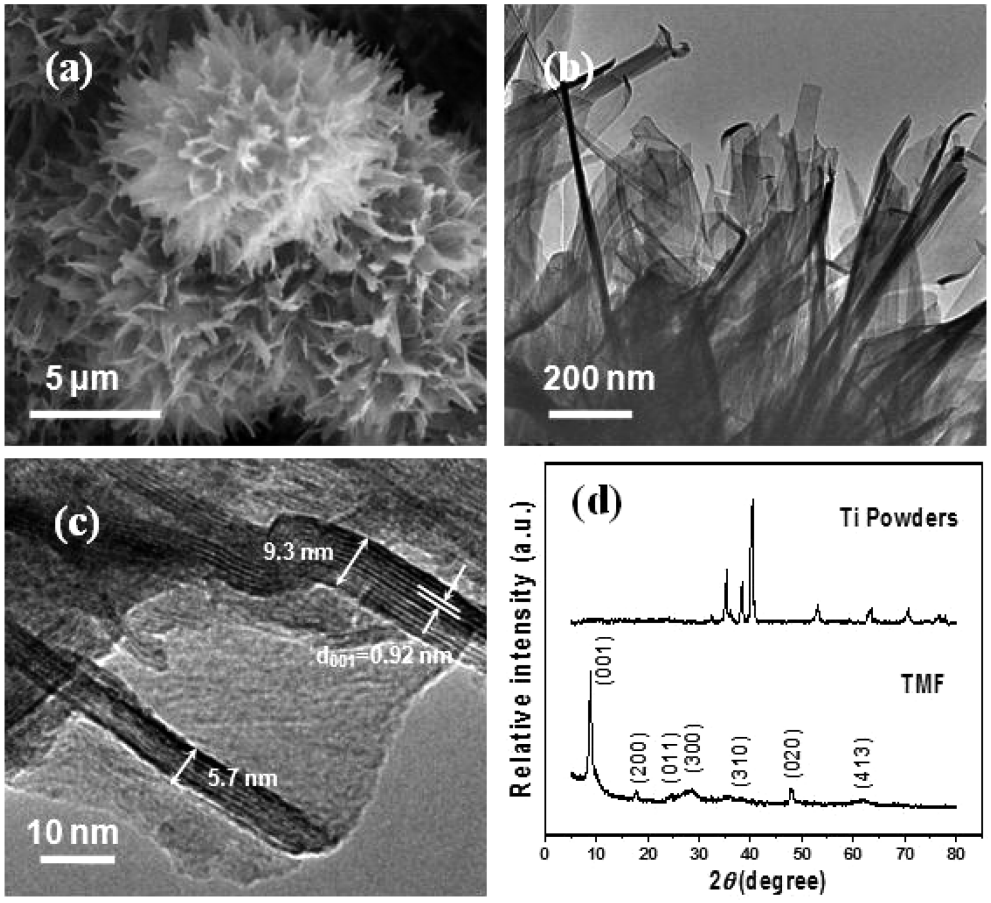

Figure 1. (a) SEM image, (b) TEM image, and (c) HRTEM image of TMF; (d) XRD patterns of metal Ti powders and TMF.

which is most commonly used for coloring paper, hair (temporary colorant), dyeing cottons, and wools.[24,25] Although MB is not regarded as acutely toxic, it has various harmful effects. On inhalation, it can give rise to short periods of rapid or difficult breathing, while ingestion through the mouth produces a burning sensation and may cause nausea, vomiting, and gastritis problems.[26,27] Therefore, it is very meaningful to research the removal of MB dye from wastewater.

Herein, we report a facile environmentally friendly hydrothermal procedure for the large-scale preparation of hierarchical sodium titanate architectures, with uniform flower-like morphologies (TMF). NaCl was used as a morphology-directing agent in a 2.0 M NaOH solution medium. TMF exhibited a high efficiency for treating dye effluents. This study provides a "green" method for preparing 3D-HTMA from Ti powder and aids our understanding of 3D-HTMA absorption applications in aqueous pollutant treatment.

MATERIALS AND METHODS

Sample Preparation. All chemicals were purchased from Sinopharm Chemical Reagent Co. Ltd., China, and used as received. Deionized water was used throughout. In a typical synthetic procedure, 0.10 g of metal Ti powders (200−300 mesh, particle size about 45−75 μm) was added to 20 mL of aqueous solution containing NaOH (2.0 M) and NaCl (4.0 M). After stirring for 15 min, the mixture was placed in a Teflon-lined vessel and then hydrothermally heated at 180 °C for 72 h. The precipitates were finally collected, washed several times with deionized water until the pH of the wash became 7, and dried in air at 50 °C.

Characterization. Scanning electron macroscopic (SEM) images were measured on a Philips XL30 model operating at a maximum accelerating voltage of 30 kV. Transmission electron microscopy (TEM) images of the samples were obtained using a Tecnai G2 F20 S-TWIN microscope. The X-ray diffraction (XRD) data were collected using a Philips XPert-MPD X-ray diffractometer with Cu Kα radiation. Nitrogen adsorption−desorption isotherms were conducted on a TriStar II 3020 (Micrometrics Instruments) surface area and pore size analyzer at 77 K. The specific surface area was calculated from the N_2 adsorption isotherm using the Brunauer−Emmett−Teller (BET) method, and the pore size distribution was determined using the Barret−Joyner−Halenda (BJH) mathematical model. Ultraviolet−visible (UV−vis) absorption spectral measurements were carried out on a Shimadzu UV-2450 spectrophotometer. Fourier transform infrared (FTIR) spectra were obtained using a Nicolet 5700 spectrometer. Raman spectra were recorded on a Renishaw 2000 Raman spectrometer (514.5 nm). ζ-Potential measurements were performed on a PALS ζ-potential analyzer.

Adsorption Experiments. The adsorption performance of the as-prepared TMF was evaluated via the adsorptive separation of MB in aqueous solution, by comparing with zero-dimensional (0D) commercially available P25 (Sigma Co., Ltd.) and 1D titanate nanobelts (TNB, prepared by a hydrothermal approach based on our previous work,[28] and see Figure S1 in the Supporting Information). All the adsorption experiments were conducted under stirring conditions throughout the test at room temperature (25 °C) in the dark. The general experimental process is described as follows: 20 mg of adsorbent (TMF, TNB, or P25) was added to 50 mL of MB solution with an initial concentration of 20 mg/L, followed by stirring at 200 rpm. At appropriate time intervals, the aliquots were withdrawn from the suspension and the adsorbents were separated from the suspension via centrifugation. The concentration of residual MB in the supernatant solution was detected using a UV−visible spectrophotometer (Shimadzu UV-2450, Japan) and was calculated from the height of the peak at 664 nm using a standard calibration curve.

Changes in total organic carbon (TOC) were determined by using a total organic carbon analyzer (Shimadzu TOC-V CPH, Japan).

RESULTS AND DISCUSSION

TMF was hydrothermally prepared in aqueous solution containing NaOH (2.0 M) and NaCl (4.0 M), at 180 °C for 72 h. A panoramic morphology of the product is presented in Figure 1a. It can be seen that the typical product morphology consisted of individually aligned 1D nanostructures. These appeared as "petals" radiating from the center, in a relatively uniform size distribution. Most petals were curved 1D nanoribbons, with a width of 100−300 nm and a length up to several hundred nanometers (Figure 1b). Figure 1c shows a HRTEM image of the ends of individual titanate nanoribbons, originating from the flower. The thicknesses of the 1D nanoribbon structures were 5−10 nm. The walls of the titanate nanoribbons consisted of several layers, and the distance between adjoining layers was ~0.92 nm. The lattice fringe revealed the presence of stacked polyanion sheets, made of interconnected [TiO_6] octahedra. XRD patterns of TMF and Ti powder are shown in Figure 1d. The absence of any Ti peaks in the TMF pattern indicated a high degree of conversion during the hydrothermal process. The XRD pattern of TMF exhibited peaks at 2θ of 8.8° (d = 1.0 nm), 17.9° (d = 0.49 nm), 24.5° (d = 0.36 nm), 28.5° (d = 0.31 nm), 38.3° (d = 0.23 nm), 47.9° (d = 0.19 nm), and 61.8° (d = 0.15 nm), which are characteristic of monoclinic $Na_2Ti_3O_7$ (JCPDS72-0148).[29] The strong narrow peak at 2$\theta \approx$ 8.8° is diagnostic of the gallery spacing for layered titanates (Figure S2 in the Supporting Information).

The N_2 adsorption−desorption isotherm of TMF indicated a specific surface area of 120.0 m^2/g from BET analysis (Figure 2). The corresponding BJH analyses (Figure 2 inset) suggested

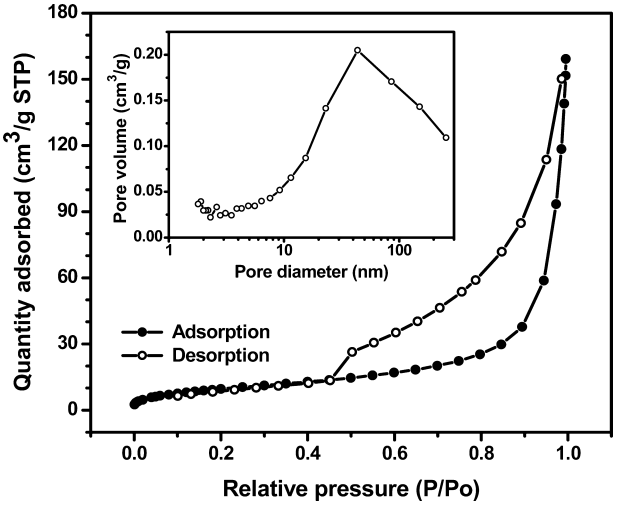

Figure 2. Typical N_2 gas adsorption−desorption isotherm of TMF. The inset is the corresponding pore size distribution.

a predominant pore diameter distribution of ~43.5 nm and a total pore volume of 0.298 cm^3/g. Pores presumably arise from the spacing between the stacked nanoribbon petals. The high BET surface area and open mesoporous morphology are likely to benefit adsorption and photocatalytic performance.[30] The BET results, along with those from SEM and TEM analyses, clearly indicated the presence of hierarchical macro/mesoporous structures in TMF.

The UV−vis absorption spectrum of TMF is depicted in Figure 3. It showed a strong absorption in the ultraviolet region

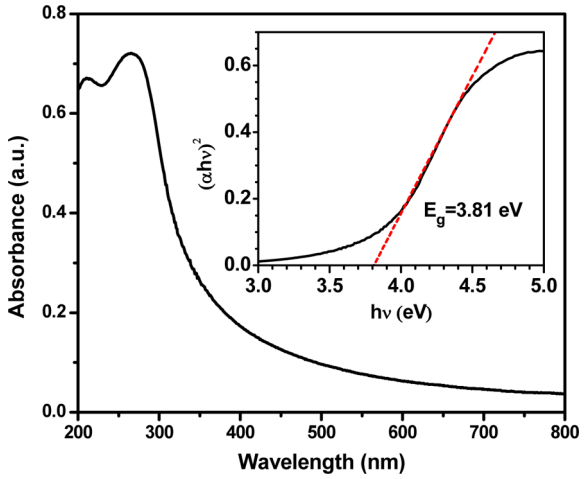

Figure 3. UV−vis absorption spectrum of TMF. Inset: Band gap (E_g) of TMF is estimated to be about 3.81 eV from the absorption edge.

near the visible-light region, due to the transition from the O^{2-}antibonding orbital to the lowest empty orbital of Ti^{4+}.[7] The energy of the band gap of TMF could be obtained from the plots of $(\alpha h\nu)^2$ versus photon energy ($h\nu$), as illustrated in Figure 3, and the value estimated from the intercept of the tangents to the plots was 3.81 eV, which is similar to the case of the reported titanate nanosheets.[31]

To understand the TMF formation mechanism, the concentration-dependent evolution of morphology was investigated from SEM measurements, as shown in Figure 4a−d. The formation of flower-like architectures depended strongly on NaCl concentration. When Ti powder was treated with a low concentration NaOH solution (without NaCl), blunt nanoplates were obtained (Figure 4a). Some nanoplates were connected, such that they appeared to be starting to form flower-like morphologies. When Ti powder was treated under similar conditions with a 2.0 M NaOH solution containing 2.0 M NaCl, a globular flower structure was observed (Figure 4b). The rough surfaces were composed of numerous uniform refined nanoplates. As the NaCl concentration increased, the core was progressively consumed, and curved nanoplates gradually transformed into nanobelts, which were longer and narrower than the nanoplates. When the NaCl concentration was 4.0 M, well-defined nanopetals of 3D-HTMA were observed, as shown in Figure 4d. The concentration-dependent SEM analyses suggested that NaCl acted as a morphology-directing agent and helped control the shape of the petals and the resulting flower-shaped structure.

The proposed growth mechanism is schematically illustrated in Scheme 1. In the initial stage of reaction, the interaction between OH^- and Ti powders leads to the dissolution of the solid particles and the formation of intermediate [TiO_6] octahedra fragments in the solution with/without NaCl. In combination with NaOH, NaCl promoted the dissolution of the titanate precursor, increasing the precursor hydrolysis rate.[32] As a result, more fragments formed, which were the building units for the 1D nanostructures. Simultaneously, addition of salt induces a lower ζ-potential of the solid surfaces and thus decreases the energy barrier of the transportation for the dissolved titanates onto a solid titanate surface.[32] We have

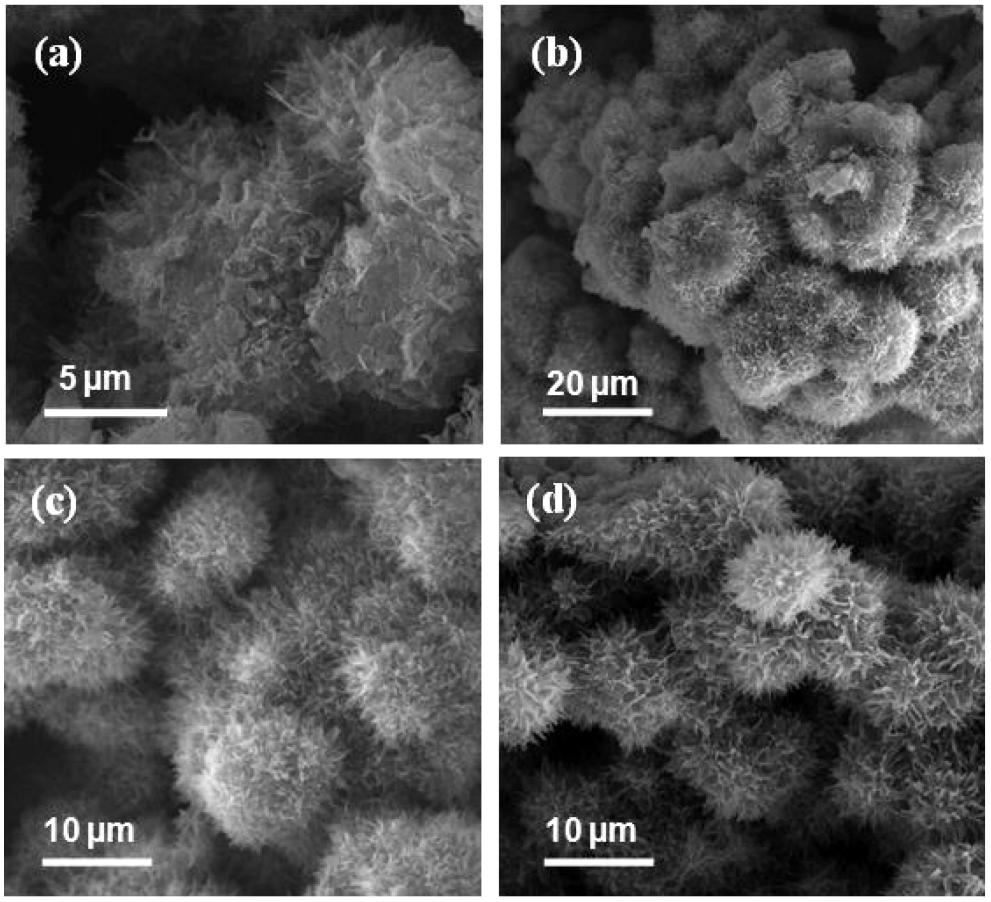

Figure 4. SEM images of NaCl concentration-dependent morphologies of flower-like titanate architectures by keeping other reaction parameters constant (0.1 g Ti powders were treated with 2.0 M NaOH at 180 °C for 72 h): (a) 0 M; (b) 2.0 M; (c) 3.0 M; and (d) 4.0 M.

Scheme 1. Schematic Growth Mechanism for the Formation of Flower-like Titanate Architectures

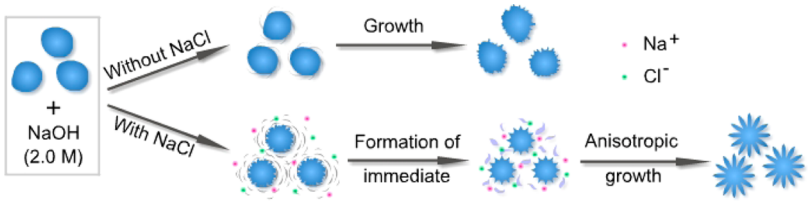

measured the ζ-potential of the sodium titanates heat-treated with varying NaCl concentration. It shows that ζ-potential became decreasingly negative from −41.23 to −28.05 mV with increasing NaCl concentration from 0 to 4.0 M (Figure 5). The decrease in the surface negative charge is consistent with our model of NaCl-assisted formation of 3D-HTMA. That is, the anisotropic growth of titanate nanocrystallites was facilitated by NaCl, which results in the final formation of flower-like sodium titanate architectures. The absence of NaCl would lead to the rough-textured particles with a few scattered blunt nanoplates. The use of NaCl was found to be crucial for the formation of flower-shaped titanate. A similar phenomenon was observed for the synthesis of pure brookite TiO_2 nanoflowers in aqueous ammonia, in which NaCl was used as an electrolyte to stabilize the layered structure of titanate.[33]

The absorption activity of TMF was demonstrated using MB. MB was removed at varying experimental conditions, as shown in Figure 6a. Adsorption occurred when TMF was added, and the characteristic absorption of MB at 664 nm decreased

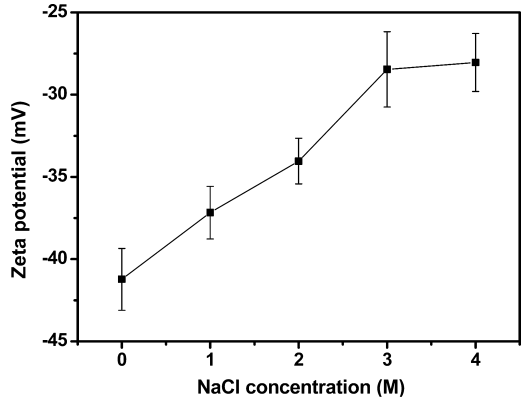

Figure 5. ζ-Potential of the sodium titanates heat-treated with varying NaCl concentration. Each data point is the mean value of three measurements with error bar of standard deviation.

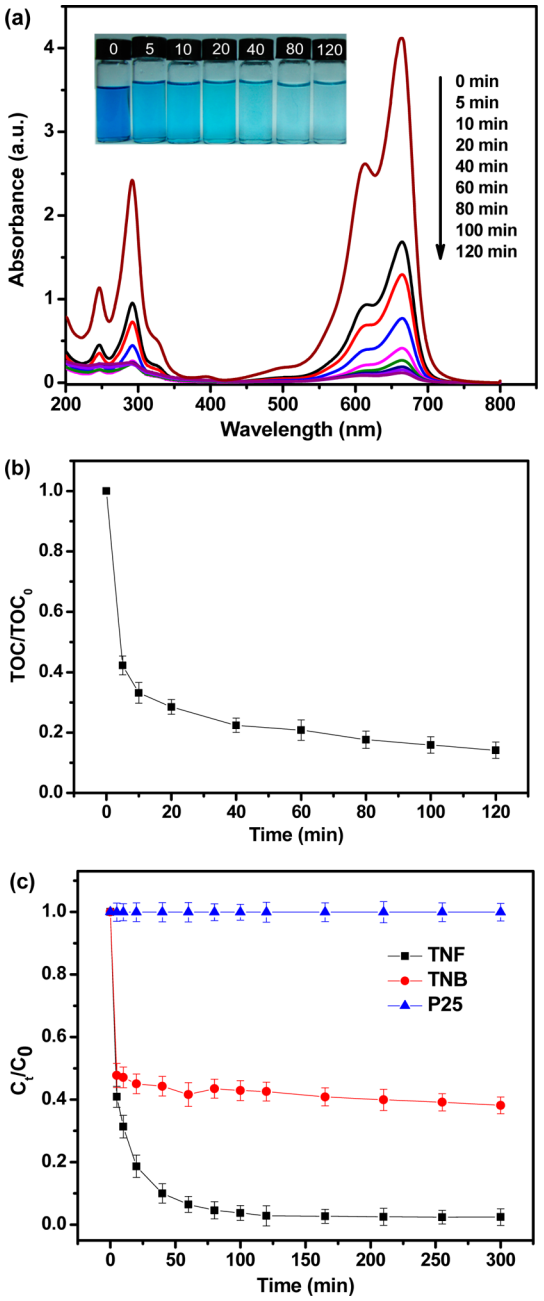

Figure 6. (a) Absorption spectra of MB solution (20 mg/L, 50 mL) in the presence of TMF (20 mg) under dark conditions. Inset represents the photograph of MB solutions at varying times. (b) TOC removal plots of MB over TMF. (c) Adsorption MB (20 mg/L, 50 mL) by TMF, TNB, and P25. C_0 is the initial concentration of the MB solution, and C is the concentration of that at different intervals during the adsorption. Error bars show standard deviations from two independent experiments, while each experiment was performed in triplicate and the average of concentrations was taken.

dramatically in the first 5 min. This was due to the strong electrostatic interaction between positively charged MB and negatively charged titanate.[34−37] Subsequently, the concentration of MB slowed down with extension of the adsorptive time, indicating that the increase of adsorption amounts with time in this stage was slower than that in the beginning stage. This is in accordance with the sample photos recorded at different times. It can be explained that the decreasing vacant surface sites became more difficult to occupy as the reaction advanced, due to repulsion between adsorbed MB molecules.[16] Moreover, measurements of TOC concentrations were adopted to assess the removal extent of an organic substrate during their radiation period. As shown in Figure 6b, TOC concentrations of the MB solutions decrease with increasing time during the reaction. It is apparent that the rate of TOC depletion is drastic in the initial stage, which is consistent with the result from UV−vis spectra. The degradation ratios in each timing period were 1.163, 0.183, 0.047, 0.031, 0.008, 0.016, 0.009, and 0.009 ppm/min, respectively. The reduced TOC of MB solution by TMF after 120 min degradation is 86%, indicating that TMF has a good capability of absorption.

The adsorption performance of TMF was compared with that of 0D P25 and 1D titanate nanobelts TNB (see Figure S3 in the Supporting Information). Figure 6c compares the changes in MB concentration with time, in the presence of these three materials. TMF removed 60% of MB from the solution after 5 min, and a 97.1% decrease in initial dye concentration was achieved after 2 h of irradiation. TNB removed 57.4% of MB after 2 h (Figure 6c and Figure S3a in the Supporting Information). Only a 0.1% reduction of the initial MB concentration was observed for P25, due to the lack of a layered structure (Figure 6c and Figure S3b in the Supporting Information). TMF exhibited the highest removal capacity and adsorption rate of MB compared with TNB and P25, which was attributed to its assembled 3D structural features and large active surface area.

In order to investigate the mechanism and characteristics of TMF adsorption in the dye removal, the adsorption kinetics model is figured out by comparing with TNB, and it relied on the adsorption breakthrough curves. The pseudo-first-order model can be expressed as

$$\ln(q_e - q_t) = \ln q_e - k_1 t \quad (1)$$

where k_1 is the Lagergren adsorption rate constant (1/min), calculated from the plots of $\ln(q_e - q_t)$ versus t for TMF and TNB (Figure 7a); q_t and q_e are the amounts of MB adsorbed (mg/g) at time t and at equilibrium, respectively. They were calculated by

$$q_t = \frac{(C_0 - C_t)V}{W} \quad (2)$$

$$q_e = \frac{(C_0 - C_e)V}{W} \quad (3)$$

where C_0 and C_e (mg/L) are the concentrations of MB at initial and equilibrium, respectively. V is the volume of the solution (L), and W is the mass of dry adsorbent used (g).

Figure 7a showed the linear plots of the pseudo-first-order kinetic model for TMF and TNB, and the kinetic parameters obtained from this model are given in Table 1. It can be seen that, although the correlation coefficient values for TMF are higher than 0.96, the calculated equilibrium adsorption capacity ($q_{e,cal}$) deviated obviously from the experimental data. It means that the applicability of this kinetic model to the adsorption of MB in this study is inappropriate.

On the other hand, higher coefficients ($R^2 > 0.99$) were achieved over both TMF and TNB in the case of the pseudo-second-order model (as shown in Figure 7b) which can be expressed as

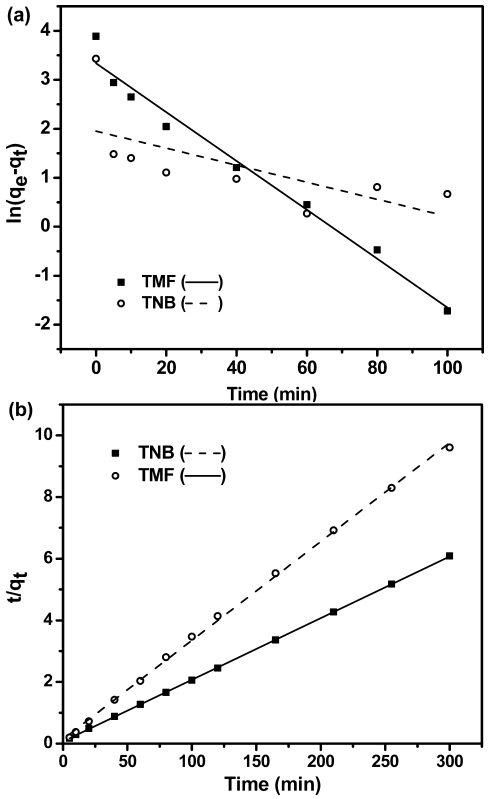

Figure 7. Adsorption kinetics models in the linear transformation for TMF and TNB for comparison: (a) pseudo-first-order and (b) pseudo-second-order.

$$\frac{t}{q_t} = \left(\frac{1}{q_e}\right)t + \frac{1}{q_e^2 k_2} \tag{4}$$

where k_2 is the pseudo-second-order rate constant (1/min). Also, the values of $q_{e,cal}$ estimated using this model were comparable with the experimentally determined values of $q_{e,exp}$, indicating the applicability of this kinetic equation. As shown in Table 1, the equilibrium removal capacity of TMF ($q_{e,cal}$ = 50.8 mg/g) is nearly twice higher than that of TNB, $q_{e,cal}$ = 31.2 mg/g. Correspondingly, TMF exhibited slow adsorption rate, typically k_2 = 0.0045 g/mg min, in comparison with 0.0073 g/mg min for TNB. Besides the value of R^2, the applicability of both kinetic models is verified through the normalized standard deviation (Δq) and uncertainty of the experimental data (namely, relative goodness of curve fitting, f). The Δq was calculated from the following equation.[38,39]

$$\Delta q\ (\%) = 100 \times \sqrt{\frac{\sum [(q_{t,exp} - q_{t,cal})/q_{t,exp}]}{n-1}} \tag{5}$$

where the $q_{t,exp}$ and $q_{t,cal}$ refer to the experimental and calculated values and n is the number of data points; f is defined according to the prediction error square (σ^2):

$$f = \frac{(\sigma^2)_{min}}{\sigma^2} \tag{6}$$

The term σ^2 is given by

$$\sigma^2 = \frac{\sum (Y_k - \hat{Y}_k)^2}{n-p} \tag{7}$$

in which Y_k and $\hat{Y}_k$ are experimental data and regressed values, and n and p are numbers of experimental data and regressed coefficients, respectively. The $(\sigma^2)_{min}$ in eq 6 is the minimum value among all σ^2 values determined by different kinetic equations.[40] The lower the value of Δq and the higher the value of f, the better will be the goodness of fit. Table 1 lists the calculated results. It was found that the adsorption of MB on TMF can be better described by the pseudo-second-order kinetic model. It is suggested that the rate of the adsorption process is controlled by the chemical adsorption, which involved valence forces through sharing or exchange of electrons between adsorbent and adsorbate.[15,41]

To probe the steps involved during adsorption, the intraparticle diffusion model was introduced to analyze the adsorption kinetic data. This model was described by external mass transfer (boundary layer diffusion) and intraparticle diffusion and had the following form:

$$q_t = k_{id} t^{0.5} + C \tag{8}$$

where k_{id} (mol/(g min$^{0.5}$)) is the diffusion coefficient and C is the boundary layer effect of the adsorption. Figure 8 presents

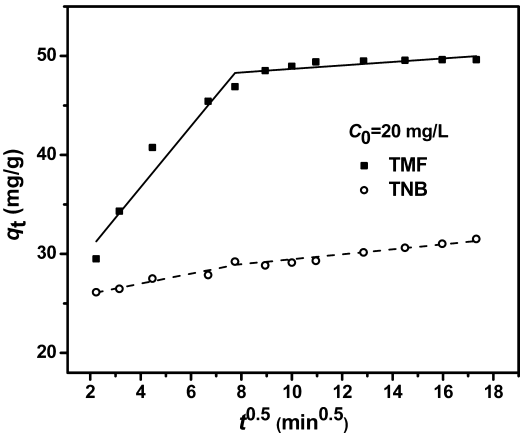

Figure 8. Diffusion model plots for the adsorption of MB on TMF and TNB.

the typical plots for the adsorption of MB on both TMF and TNB using the diffusion model. As shown in Figure 8, two-

Table 1. Comparison of the Pseudo-First- and Second-Order Adsorption Rate Constants and Calculated and Experimental, q_e, Values for TMF and TNB

		first-order kinetic model					second-order kinetic model				
samples	$q_{e,exp}$ (mg/g)	k_1 (g/mg min)	$q_{e,cal}$ (mg/g)	R^2	Δq (%)	f	k_2 (g/mg min)	$q_{e,cal}$ (mg/g)	R^2	Δq (%)	f
TMF	49.3	0.0390	24.9	0.9623	13.2	0.87	0.0045	50.8	0.9999	2.4	0.98
TNB	30.8	0.0158	7.3	0.7707	21.7	0.69	0.0073	31.2	0.9990	3.6	0.91

dx.doi.org/10.1021/am404011k | ACS Appl. Mater. Interfaces 2013, 5, 12654−12662

stage adsorption was shown distinctly for MB adsorbed on TMF, which suggests that the adsorption process proceeds by surface adsorption and intraparticle diffusion. The initial curved portion of the plot indicates a boundary layer effect, while the second linear portion is due to intraparticle or pore diffusion. The linear plot of the second portion of q_t versus $t^{0.5}$ did not pass through the origin, and the intercept was 46.9 and 26.9 mg/g, respectively. This implied that the overall rate of the dye adsorption process was controlled by both surface adsorption and intraparticle diffusion. A similar phenomenon was observed for the adsorption of MB from aqueous solution on titanate nanoflowers,[16] titanate nanotubes,[41] clay,[42] and 3D grapheme oxide.[43]

In order to determine the actual rate-controlling step involved in the dye adsorption process, the adsorption kinetic data were further analyzed using Boyd kinetic expression as follows:[44]

$$B_t = -0.4977 - \ln\left(1 - \frac{q_t}{q_e}\right) \quad (6)$$

Figure 9 shows the calculated B_t values against t or TMF and TNB. It is evident that the plots are not straight lines to pass

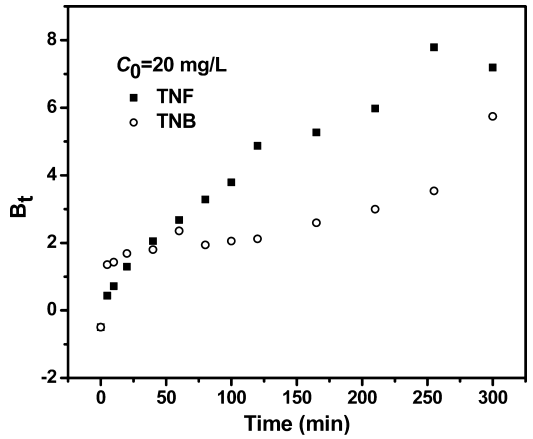

Figure 9. Correlation between B_t and t for the adsorption of MB onto TMF and TNB.

the origin, implying external mass transport mainly governs the rate-limiting process.

The abundance of MB adsorbed in TMF can be confirmed by means of FTIR and Raman scattering spectroscopy. As shown in Figure 10a, the FTIR spectrum of the TMF displays two bands from 1300 to 1700 cm^{-1}. The characteristic bands at 1628 and 1385 cm^{-1} were assigned to H−O−H binding vibration and the Ti−O vibrations, respectively.[34,41] The broad absorption peak at 3386 cm^{-1} was attributed to stretching vibrational aspect of Ti−OH bands,[45] while the shoulder at 3218 cm^{-1} from Ti−OH bonds was ascribed to the strong interaction between Ti ions and OH groups.[46] After adsorption of MB by TMF (TMF-MB for short), the characteristic spectrum of MB, such as its ring stretch at 1603 cm^{-1},[47] the symmetric stretch of C−N at 1489 and 1398 cm^{-1}, and symmetric deformation of $-CH_3$ at 1354 and 1340 cm^{-1},[8] was recorded in the spectrum of the adsorptive adduct (Figure 10a, top). This reflected the evidence for the strong interaction between MB and TMF.

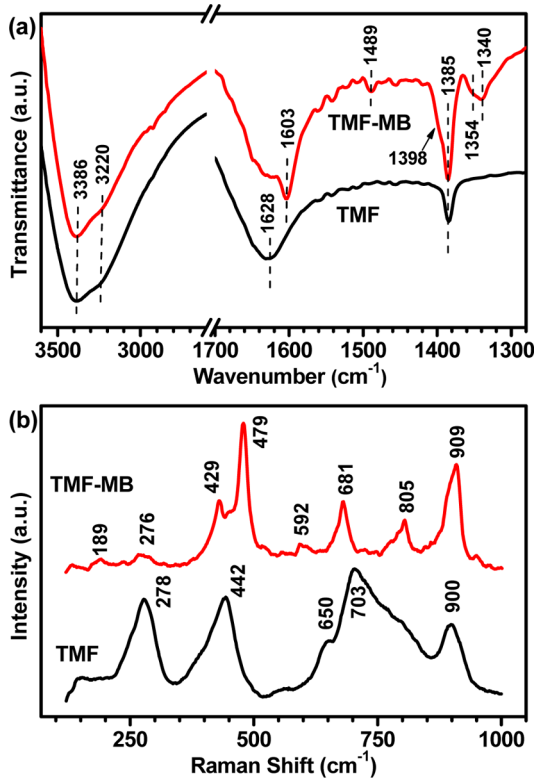

Figure 10. (a) FTIR and (b) Raman spectra of TMF before and after the absorption of MB.

Raman spectra of the samples before and after the absorption of MB are shown in Figure 9b. For the as-prepared TMF (Figure 10b, bottom), the Raman spectrum at room temperature revealed broad bands at 278, 442, 650, 703, and 900 cm^{-1} (Figure 10b, bottom), which were mainly the Ti−O lattice vibrations. For instance, the Raman bands at 278 and 442 cm^{-1} correspond to the Na−O−Ti stretching and framework Ti−O−Ti vibrations, respectively.[48] The Raman bands at 650 and 703 cm^{-1} have generally been attributed to the Ti−O−Ti stretch in edge-shared TiO_6 octahedra.[49] The band at 900 cm^{-1} has been recognized as the symmetric stretch of short Ti−O bonds involving nonbridging oxygen atoms associated with sodium ions.[3,4,50] As MB is absorbed, this peak shifts to higher frequencies around 909 cm^{-1}, while the peaks near 650 and 703 cm^{-1} just disappear after the absorption of MB, indicating that the adsorption could mainly have occurred through the interaction between MB and Ti−O groups of the TMF (Figure 10b, top). The two peaks at 429 and 479 cm^{-1} in the TMF-MB spectra are assigned to C−N−C skeletal bending vibration of MB.[51] Furthermore, several of the bands belonging to MB have a little shift in position upon adsorption onto the TMF, such as the peaks at 677 and 768 cm^{-1} in free MB that shift to 681 and 805 cm^{-1}, respectively. It is noticeable that two additional Raman bands show up in the TMF-MB spectra, namely, 189 and 592 cm^{-1}. Similar to the conclusion drawn from the FTIR spectra, the adsorption of MB onto the TMF was also substantial, based on the Raman spectra. On the other hand, the splits and shifts of a few Raman bands imply that MB molecules may be chemisorbed onto the surface and intercalated into the interlayer spacing of TMF, so chemical effects are the main mechanism responsible for the relative shifts.

The above demonstrations provide further evidence of the absorption of MB onto the TMF, and the observed changes in the FTIR and Raman spectra are generally consistent with the chemical adsorption kinetics model. Then it was believed that the formation of the MB-TMF composite occurred, similar to the previous reports, where the MB-TNT and MB-SWNT nanocomposites were formed when MB was adsorbed onto TNTs and SWNTs, respectively.[41,47]

Moreover, two other organic dyes with different charges (methyl orange and rhodamine B) were used as model compounds to evaluate the adsorption selectivity of the as-prepared TMF. The result shows that most (~93%) MB was removed after 120 min, whereas there was little change for methyl orange and a slight decrease for rhodamine B in the absorption spectra (Figure S4 in the Supporting Information). As the surface is dominated by negative charges, TMF presents good selectivity toward positive organic groups because of the electrostatic attraction. This explains why methyl orange could not be adsorbed on TMF because methyl orange molecules are negatively charged. The positively charged MB and rhodamine B can be adsorbed. Nevertheless, previous study reveals that for such layered titanate the contribution of adsorption from the interspace surface is greater than that from the outer surface.[52] An effective adsorption depends on the ability to embed the dye molecules into the interspaces between titanate layers. Structurally, the molecule size of rhodamine B is much bigger than MB (insets in Figure S4a,c), which results in the ineffective adsorption of rhodamine B. Consequently, only the positively charged MB could be embedded in the layer interspaces of TMF through ion exchange.

CONCLUSION

In summary, an easy and environmentally friendly hydrothermal procedure for preparing flower-like layered sodium titanate architectures was reported. NaCl was used as a morphology-directing agent in a weakly alkaline medium. A growth mechanism was proposed. TMF exhibited excellent removal capability toward methylene blue, suggesting its potential in treating contaminated wastewater. This procedure has potential in fabricating further functional hierarchical architectures because it allows a high degree of control over their structure and morphology.

ASSOCIATED CONTENT

Supporting Information

(1) TEM image of TNB (Figure S1), (2) structures of $Na_2Ti_3O_7$ (Figure S2), (3) absorption spectra of MB solution in the presence of TNB and P25 under dark conditions (Figure S3), and (4) absorption spectra of MB, methyl orange, and rhodamine B before and after treated with TMF under dark conditions for 120 min (Figure S4). This material is available free of charge via the Internet at http://pubs.acs.org.

AUTHOR INFORMATION

Corresponding Author

*Tel: +86-591-22866540. Fax: +86-591-22866539. E-mail: hbzhan@fzu.edu.cn.

Notes

The authors declare no competing financial interest.

ACKNOWLEDGMENTS

This study was financially supported by National Natural Science Foundation of China (No. 51172045), Specialized Research Fund for the Doctoral Program of Higher Education of China (No. 20113514120006), and Natural Science Foundation of Fujian Province (No. 2012J05113). The authors thank Key Laboratory for Subtropical Mountain Ecology (Funded by Ministry of Science and Technology and Fujian Province), Fuzhou 350007, for TOC testing.

REFERENCES

(1) Grandcolas, M.; Louvet, A.; Keller, N.; Keller, V. *Angew. Chem., Int. Ed.* **2009**, *48*, 161−164.
(2) Yang, D. J.; Zheng, Z. F.; Zhu, H. Y.; Liu, H. W.; Gao, X. P. *Adv. Mater.* **2008**, *20*, 2777−2781.
(3) Li, N.; Zhang, L. D.; Chen, Y. Z.; Fang, M.; Zhang, J. X.; Wang, H. M. *Adv. Funct. Mater.* **2012**, *22*, 835−841.
(4) Liu, J. H.; Chen, J. S.; Wei, X. F.; Lou, X. W.; Liu, X. W. *Adv. Mater.* **2011**, *23*, 998−1002.
(5) Wang, C. X.; Yin, L. W.; Zhang, L. Y.; Qi, Y. X.; Lun, N.; Liu, N. N. *Langmuir* **2010**, *26*, 12841−12848.
(6) Bavykin, D. V.; Friedrich, J. M.; Walsh, F. C. *Adv. Mater.* **2006**, *18*, 2807−2824.
(7) Mao, Y. B.; Wong, S. S. *J. Am. Chem. Soc.* **2006**, *128*, 8217−8226.
(8) Riss, A.; Berger, T.; Stankic, S.; Bernardi, J.; Knözinger, E.; Diwald, O. *Angew. Chem., Int. Ed.* **2008**, *47*, 1496−1499.
(9) Zhang, L.; Zhang, Q.; Li, J. H. *Adv. Funct. Mater.* **2007**, *17*, 1958−1965.
(10) Dinh, C. T.; Seo, Y.; Nguyen, T. D.; Kleitz, F.; Do, T. O. *Angew. Chem., Int. Ed.* **2012**, *51*, 6608−6612.
(11) Okada, K.; Tokudome, Y.; Falcaro, P.; Takamatsu, Y.; Nakahira, A.; Takahashi, M. *Chem. Commun.* **2012**, *48*, 6130−6132.
(12) Zhu, T. J.; Li, J.; Wu, Q. S. *ACS Appl. Mater. Interfaces* **2011**, *3*, 3448−3453.
(13) Li, J. M.; Wan, W.; Zhu, F.; Li, Q.; Zhou, H. H.; Li, J. J.; Xu, D. S. *Chem. Commun.* **2012**, *48*, 389−391.
(14) Sun, Z. Q.; Kim, J. H.; Zhao, Y.; Attard, D.; Dou, S. X. *Chem. Commun.* **2013**, *49*, 966−968.
(15) Huang, J. Q.; Cao, Y. G.; Liu, Z. G.; Deng, Z. H.; Tang, F.; Wang, W. C. *Chem. Eng. J.* **2012**, *180*, 75−80.
(16) Huang, J. Q.; Cao, Y. G.; Liu, Z. G.; Deng, Z. H.; Wang, W. C. *Chem. Eng. J.* **2012**, *191*, 38−44.
(17) Yu, J. G.; Li, Q. L.; Fan, J. J.; Cheng, B. *Chem. Commun.* **2011**, *47*, 9161−9163.
(18) Peng, X. S.; Chen, A. C. *Adv. Funct. Mater.* **2006**, *16*, 1355−1362.
(19) Wu, J. M.; Song, X. M.; Yan, M. *J. Hazard. Mater.* **2011**, *194*, 338−344.
(20) Zhu, J.; Wang, S. H.; Bian, Z. F.; Cai, C. L.; Li, H. X. *Res. Chem. Intermed.* **2009**, *35*, 769−777.
(21) Huang, J. Q.; Huang, Z.; Guo, W.; Wang, M. L.; Cao, Y. G.; Hong, M. C. *Cryst. Growth Des.* **2008**, *8*, 2444−2446.
(22) Tang, Y. X.; Gong, D. G.; Lai, Y. K.; Shen, Y. Q.; Zhang, Y. Y.; Huang, Y. Z.; Tao, J.; Lin, C. J.; Dong, Z. L.; Chen, Z. *J. Mater. Chem.* **2010**, *20*, 10169−10178.
(23) Tang, Y. F.; Yang, L.; Chen, J. Z.; Qiu, Z. *Langmuir* **2010**, *26*, 10111−10114.
(24) Hameed, B. H.; Din, A. T. M.; Ahmad, A. L. *J. Hazard. Mater.* **2007**, *141*, 819−825.
(25) Song, J. Y.; Zou, W. H.; Bian, Y. Y.; Su, F. Y.; Han, R. P. *Desalination* **2011**, *265*, 119−125.
(26) Özer, D.; Dursun, G.; Özer, A. *J. Hazard. Mater.* **2007**, *144*, 171−179.
(27) Özer, A.; Dursun, G. *J. Hazard. Mater.* **2007**, *146*, 262−269.
(28) Feng, M.; Zhan, H. B.; Miao, L. *ACS Appl. Mater. Interfaces* **2010**, *2*, 1129−1135.

(29) Zhang, Z.; Goodall, J. B. M.; Brown, S.; Karlsson, L.; Clark, R. J. H.; Hutchison, J. L.; Rehman, I. U.; Darr, J. A. *Dalton Trans.* **2010**, *39*, 711−714.
(30) Zhai, Q. Q.; Bo, T.; Hu, G. X. *J. Hazard. Mater.* **2011**, *128*, 78−86.
(31) Sakai, N.; Ebina, Y.; Takada, K.; Sasaki, T. *J. Am. Chem. Soc.* **2004**, *126*, 5851−5858.
(32) Li, J.; Zhou, Z. X.; Zhu, L. H.; Xu, K.; Tang, H. Q. *J. Phys. Chem. C* **2007**, *111*, 16768−16773.
(33) Zhao, B.; Chen, F.; Huang, Q. W.; Zhang, J. L. *Chem. Commun.* **2009**, *34*, 5115−5117.
(34) Lim, Y. W. L.; Tang, Y. X.; Cheng, Y. H.; Chen, Z. *Nanoscale* **2010**, *2*, 2751−2757.
(35) Tang, Y. X.; Jiang, Z. L.; Tay, Q. L.; Deng, J.; Lai, Y. K.; Gong, D. G.; Dong, Z. L.; Chen, Z. *RSC Adv.* **2012**, *2*, 9406−9414.
(36) Xie, S. F.; Zheng, B. J.; Kuang, Q.; Wang, X.; Xie, Z. X.; Zheng, L. S. *CrystEngComm* **2012**, *14*, 7715−7720.
(37) Ma, J.; Yu, F.; Zhou, L.; Jin, L.; Yang, M. X.; Luan, J. S.; Tang, Y. H.; Fan, H. B.; Yuan, Z. W.; Chen, J. H. *ACS Appl. Mater. Interfaces* **2012**, *4*, 5749−5760.
(38) Weng, C. H.; Lin, Y. T.; Tzeng, T. W. *J. Hazard. Mater.* **2009**, *170*, 417−424.
(39) Nasuha, N.; Hameed, B. H.; Din, A. T. *J. Hazard. Mater.* **2010**, *175*, 126−132.
(40) Liu, Y.; Wang, Z. W. *Bioresour. Technol.* **2008**, *99*, 3309−3312.
(41) Xiong, L.; Yang, Y.; Mai, J. X.; Sun, W. L.; Zhang, C. Y.; Wei, D. P.; Chen, Q.; Ni, J. R. *Chem. Eng. J.* **2010**, *156*, 313−320.
(42) Gurses, A.; Dogar, C.; Yalcin, M.; Acikyildiz, M.; Bayrak, R.; Karaca, S. *J. Hazard. Mater.* **2006**, *131*, 217−228.
(43) Liu, F.; Chung, S.; Oh, G.; Seo, T. S. *ACS Appl. Mater. Interfaces* **2012**, *4*, 922−927.
(44) Lee, C. K.; Lin, K. S.; Wu, C. F.; Lyu, M. D.; Lo, C. C. *J. Hazard. Mater.* **2008**, *150*, 494−503.
(45) Wang, C. X.; Yin, L. W.; Zhang, L. Y.; Liu, N. N.; Lun, N.; Qi, Y. X. *ACS Appl. Mater. Interfaces* **2010**, *2*, 3373−3377.
(46) Erjavec, B.; Kaplan, R.; Djinović, P.; Pintar, A. *Appl. Catal., B* **2013**, *132*−*133*, 342−352.
(47) Yan, Y. M.; Zhang, M. N.; Gong, K. P.; Su, L.; Guo, Z. X.; Mao, L. Q. *Chem. Mater.* **2005**, *17*, 3457−3463.
(48) Gao, T.; Fjellvåg, H.; Norby, P. *Inorg. Chem.* **2009**, *48*, 1423−1432.
(49) Kitano, M.; Wada, E.; Nakajima, K.; Hayashi, S.; Miyazaki, S.; Kobayashi, H.; Hara, M. *Chem. Mater.* **2013**, *25*, 385−393.
(50) Yin, J.; Qi, L.; Wang, H. Y. *ACS Appl. Mater. Interfaces* **2012**, *4*, 2762−2768.
(51) Xiao, G. N.; Man, S. Q. *Chem. Phys. Lett.* **2007**, *447*, 305−309.
(52) Xie, S. F.; Zheng, B. J.; Kuang, Q.; Wang, X.; Xie, Z. X.; Zheng, L. S. *CrystEngComm* **2012**, *14*, 7715−7720.